ORIGINAL PAPER

Trace element and isotopic zoning of garnetite veins in amphibolitized eclogite, Franciscan Complex, California, USA

Alicia M. Cruz-Uribe[1,2] · F. Zeb Page[3] · Emilie Lozier[3] · Maureen D. Feineman[2] · Thomas Zack[4] · Regina Mertz-Kraus[5] · Dorrit E. Jacob[6] · Kouki Kitajima[7]

Abstract

Here we present major element, trace element, and oxygen isotope data for garnet from an amphibolitized eclogite block from Ring Mountain, Franciscan Complex, California, USA. Garnetite veins 1–5 cm thick are laterally continuous up to 10 m within an Mg-rich blackwall zone of the eclogite block. Complex major and trace element zoning patterns reveal multiple stages of garnet growth in both the matrix and garnetite veins. Similarities in major and trace element zoning between matrix and vein garnet suggest that crystallization of the garnetite veins began toward the end of matrix garnet core growth, and continued throughout the garnet growth history of the rock. Oscillatory zoning in rare-earth elements suggests garnet growth in pulses, with matrix-diffusion-limited growth in between pulses. Oxygen isotope analyses of matrix and vein garnet have a range in $\delta^{18}O$ values of 5.3–11.1 ‰. Differences in $\delta^{18}O$ values of up to ~ 4 ‰ between garnet core and rim are observed in both the matrix and vein; garnet cores range from 9.8 to 11.1 ‰ (median 10.4‰), garnet mantles range from 8.3 to 10.0 ‰ (median 9.7 ‰), and garnet rims range from 5.8 to 7.8 ‰ (median 6.7 ‰). Late-stage vein crystallization appears as a garnet "cement" that fills in a network of small (typically 5–50 µm) garnet cores, and likely crystallized from an amorphous phase. The low $\delta^{18}O$ values of this latest stage of garnet growth are consistent with interaction with serpentinites, and likely represent the physical incorporation of the eclogite block into the serpentinite matrix mélange.

Communicated by Daniela Rubatto.

✉ Alicia M. Cruz-Uribe
  alicia.cruzuribe@maine.edu

1   School of Earth and Climate Sciences, University of Maine, 5790 Bryand Global Sciences Center, Orono, ME 04469, USA

2   Department of Geosciences, The Pennsylvania State University, 542 Deike Building, University Park, PA 16802, USA

3   Department of Geology, Oberlin College, 52 West Lorain St., Oberlin, OH 44074, USA

4   Department of Earth Sciences, University of Gothenburg, Guldhedsgatan 5A, Box 460, 40530 Gothenburg, Sweden

5   Institute for Geosciences, Johannes Gutenberg University, J.-J. Becher Weg 21, 55128 Mainz, Germany

6   Department of Earth and Planetary Sciences, Macquarie University, Sydney, NSW 2109, Australia

7   Department of Geoscience, University of Wisconsin, Madison, WI 53706, USA

Introduction

Many minerals record information about the pressure (*P*), temperature (*T*), time (*t*), composition (*X*), and deformation (*D*) history of rocks. Of these, garnet is one of the most ubiquitous. Numerous workers have used trace element (e.g., Hickmott et al. 1987; Otamendi et al. 2002; Pyle and Spear 2003; Yang and Rivers 2004; Skora et al. 2006; Rubatto et al. 2020) and stable isotope (e.g., Kohn and Valley 1994; Jacob 2004; Page et al. 2010, 2014; Russell et al. 2012; Martin et al. 2014; Rubatto and Angiboust 2015) compositions in garnet to unravel rock-forming processes in subduction zones and other metamorphic environments. The distribution and zoning of rare-earth elements (REE) in garnet have been used widely to track changes in the reactive assemblage during garnet growth (Konrad-Schmolke et al. 2006, 2008; Moore et al. 2013), and interpret geochronology in the Lu–Hf and Sm–Nd systems (Anczkiewicz et al. 2007; Kelly et al. 2011; Smit et al. 2013; Cruz-Uribe et al. 2015).

In situ analyses of oxygen isotope ratios in garnet have been extensively used to elucidate fluid histories in metamorphic rocks (e.g., Russell et al. 2012; Martin et al. 2014; Page et al. 2014; Rubatto and Angiboust 2015; Vho et al. 2020b), including during extreme metamorphic events (e.g., Vielzeuf et al. 2005; Page et al. 2010). Many orogenic eclogites show minimal core-rim zoning in $\delta^{18}O$, with core-rim variations of ~1.5–2.5 ‰ (Russell et al. 2012). However, core-rim variations in $\delta^{18}O$ on the order of 3–10 ‰ have been reported in high-pressure garnet (Errico et al. 2013; Martin et al. 2014; Page et al. 2014, 2019; Rubatto and Angiboust 2015) and are interpreted as records of metasomatic fluid interactions.

The focus of this study is the geochemistry of garnetite veins (Fig. 1) in an amphibolitized eclogite from the Tiburon Peninsula, Franciscan subduction complex, California. We use major and trace element zoning in conjunction with oxygen isotopes in garnet to track the origin and evolution of fluids during mélange formation. Matrix garnet cores and initial vein chemistry suggest that early fluids were internally derived, whereas lower-$\delta^{18}O$ vein garnet and matrix garnet rims point to an external fluid source, likely coincident with the breakup of the high-grade block and incorporation into the serpentinite mélange.

The subduction interface is a critically important region whereby the physical and chemical mixing of subducted oceanic crust, slab-top sediments, and the mantle wedge promotes the formation of hybrid, or mélange, rocks (Cloos and Shreve 1988; Bebout and Barton 2002; Miller et al. 2009; Marschall and Schumacher 2012). One of the characteristic features of many mélange zones is the formation of a block-and-matrix texture, which preserves often high-grade blocks within serpentinite, chlorite, and/or sedimentary matrix. The reaction rinds on high-grade blocks are often intensely hydrated zones consisting of amphibole, mica, and epidote (Sorensen and Grossman 1993; Penniston-Dorland et al. 2010; Bebout and Penniston-Dorland 2016). In the Franciscan, and elsewhere, these reaction rinds are typically Mg-rich and are dominated by actinolite, talc, and high-Si white mica, and have been interpreted to be the result of metasomatism associated with the serpentinization of ultramafic rocks within the subduction channel (Nelson 1995; Catlos and Sorensen 2003; Horodyskyj et al. 2009).

Geologic setting and sample description

The Jurassic Franciscan Complex of coastal California consists of high-grade blocks of amphibolite, eclogite, and blueschist within a tectonic mélange composed primarily of serpentinite and shale (Wakabayashi 1990). Most Franciscan high-grade blocks are proposed to have counterclockwise pressure–temperature (*P–T*) paths, with early epidote–amphibolite-facies metamorphism followed by peak eclogite-facies metamorphism and finally blueschist-facies overprinting (Wakabayashi 1990; Tsujimori et al. 2006; Page et al. 2007). Eclogite blocks from Ring Mountain (Tiburon Peninsula) record peak pressures of 2.2–2.5 GPa and temperatures of 550–620 °C, followed by blueschist-facies overprinting between ~1–2 GPa and ~300–500 °C (Tsujimori et al. 2006). Amphibolite blocks generally fall into two categories: those that were early amphibolites later overprinted by eclogite- and then blueschist-facies assemblages (Wakabayashi 1990; Tsujimori et al. 2006), and eclogites that were overprinted by amphibolite and then blueschist-facies assemblages (Mulcahy et al. 2018). This second type of amphibolite may indicate a clockwise *P–T* history (Mulcahy et al. 2018).

Samples RM-1C (Cruz-Uribe et al. 2018) and 13TIB3 are from an amphibolitized eclogite block ~15×30 m in size from the Ring Mountain locality on the Tiburon Peninsula (IGSN: IEOMG0010). This high-grade block is found within a serpentinite matrix mélange (Brothers 1954; Bero 2014) and is the same block from which sample EA (IGSN: IESRM0002) was reported by Mulcahy et al. (2018). Mulcahy et al. (2018) reported garnet Lu–Hf ages for matrix garnet with a minimum age of initial garnet growth of 166±1 Ma and a maximum age of final garnet growth of 155±1 Ma. They also reported zircon U–Pb weighted mean ages of 176±4 Ma for zircon enclosed within garnet, which is interpreted as the timing of the eclogite formation, and 160±4 Ma for zircon within the matrix, which records the amphibolite overprint (Mulcahy et al. 2018). Though noted by the authors, Mulcahy et al. (2018) specifically did not sample the garnetite veins in this block for geochronology.

Samples RM-1C and 13TIB3 are from an amphibolitized zone of the eclogite block. The primary phases are garnet, calcic amphibole, omphacite, high-Si white mica, apatite, zoisite, and rutile. Matrix rutile is partially altered to titanite, and hornblende is partially replaced by glaucophane. Euhedral titanite is also present in the matrix in association with chlorite and is interpreted to be part of the late blueschist overprint (Fig. S1). Garnet occurs both as matrix porphyroblasts (2–5 mm) and as small grains (5–50 µm) in thick (1–5 cm) garnetite veins that are laterally continuous up to ~10 m across the outcrop (Fig. 1a–d). Garnet in the garnetite veins shows clear core, mantle, and rim zones in BSE (Figs. 1h and S3), and the rims of the garnet form a "cement" that links together the interiors of the vein garnet grains (Fig. 1g). In the case of the garnetite vein analyzed in 13TIB3 (Fig. 1d), the rim "cement" also makes up a low-BSE zone at the edge of the vein. A medium-sized (hundreds of µm) population of garnet occurs at the edges of the veins; these are henceforth referred to as vein-edge garnet (Fig. 1e, f). Many of the vein-edge garnet grains have square or rectangular cross sections (Figs. 1, 2, S5, S8 and S10). Garnetite veins consist primarily of garnet (95 % by volume)
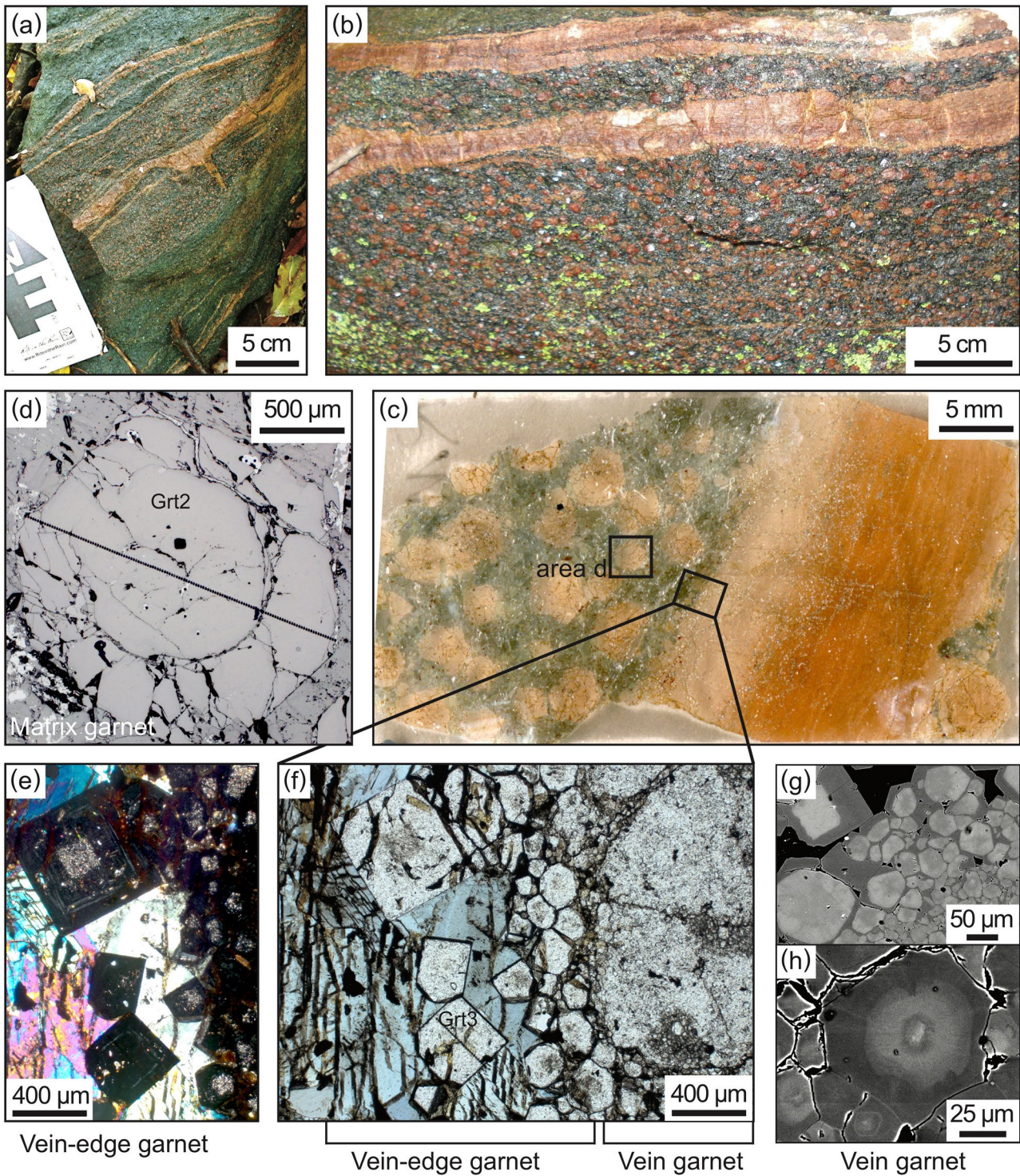
Fig. 1 Field photos and thin section images of garnetite veins in amphibolitized eclogite block, Ring Mountain, California. **a**, **b** Outcrop photos of garnetite veins. **c** Scan of thin section of sample RM-1C showing locations of various highlighted sections. **d** Reflected light photo of RM-1C matrix Grt2. **e** Cross-polarized light (XPL) photo of vein-edge garnets shown in (**f**). **f** Plane polarized light photo (PPL) of vein-edge garnet and vein garnet in sample RM-1C. **g** Backscattered electron (BSE) image of vein garnet showing cores surrounded by low-BSE garnet "cement" in sample 13TIB3. **h** BSE image of vein garnet showing clear core, mantle, and rim textures in sample RM-1C
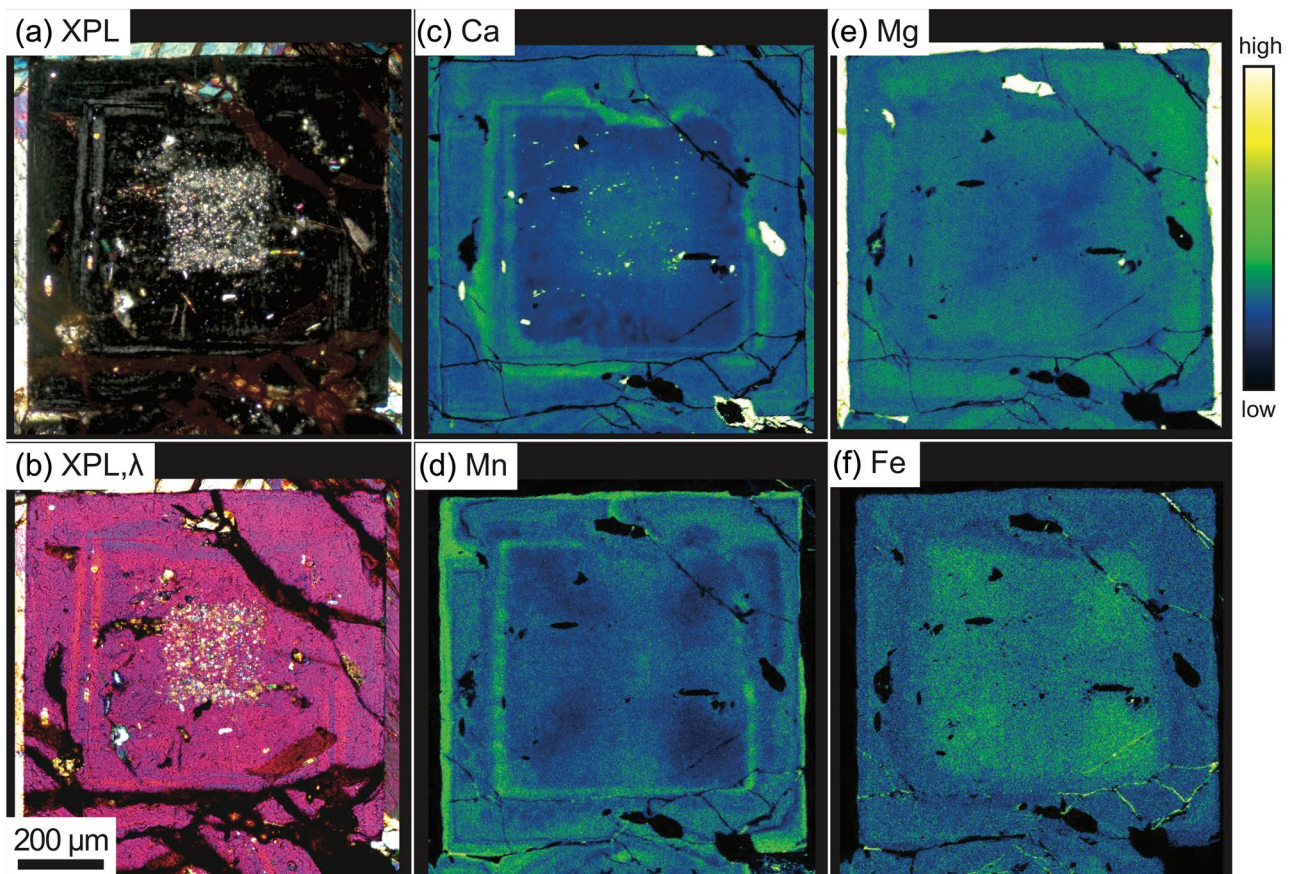
Fig. 2 Photomicrographs highlighting optical anisotropy and WDS major element maps of vein-edge Grt6, sample RM-1C. **a** XPL. **b** XPL with lambda plate inserted. **c** Ca map. **d** Mn map. **e** Mg map. **f** Fe map. Green indicates higher concentrations and blue indicates lower concentrations here and in subsequent figures

with minor amounts of rutile, white mica, amphibole, zircon, and sulfides (chalcopyrite and pyrrhotite). The garnetite veins themselves are zoned chemically, as evidenced by the difference in color across the vein (Figs. 1b, c, S2 and S7). All of the garnet grains in this study contain zones that exhibit optical anisotropy (birefringence); this is particularly noticeable in the vein and vein-edge garnet (Fig. 2a, b).

Analytical methods

Electron beam instrumentation

Garnet major element maps for RM-1C Grt2, Grt3, Grt4, and 13TIB3 GrtD, GrtG, were produced using an EDAX Pegasus energy-dispersive spectrometry (EDS) system on the Tescan Vega II XMU scanning electron microscope at the University of Maine. Conditions for EDS maps were 20 kV accelerating voltage with a probe current of ~ 500–700 nA, and a dwell time of 100 ms. Garnet major element maps for RM-1C Grt5 and Grt6 were produced by electron probe

microanalysis (EPMA) using a CAMECA SX100 at Rensselaer Polytechnic Institute with an accelerating voltage of 15 kV using a focused beam, a beam current of 100 nA, a dwell time of 0.03 s, and a step size of 2 μm. Major element maps were processed using XMapTools to correct for intensity drift during map acquisition (Lanari et al. 2014, 2018). Final images were processed using ImageJ.

Major element concentrations in garnet, amphibole, and white mica in sample RM-1C were determined by EPMA using a CAMECA SX100 at Rensselaer Polytechnic Institute. Major element concentrations in garnet in samples RM-1C and 13TIB3 were determined by EPMA using a CAMECA SX100 at the University of Michigan. A focused beam was used with an accelerating voltage of 15 keV and a beam current of 20 nA for analyses on both instruments. Calibration was done using natural and synthetic silicate and oxide standards, and a CAMECA PAP-type correction was applied. Dwell times for Mg, Al. Cr, V, Mn, and Si were 20 s on peak and 10 s each on high and low backgrounds, and for Ti and Fe were 10 s on peak and 5 s each on high and low backgrounds. Backgrounds were measured at every point.

Laser ablation inductively coupled plasma mass spectrometry

Trace element concentrations in garnet were determined by laser ablation-inductively coupled plasma-mass spectrometry (LA-ICP-MS) at the University of Mainz, Germany (sample RM-1C), and the University of Maine, USA (sample 13TIB3). Values for reference glasses were taken from the Max Planck Institute GeoReM database (http://georem. mpch-mainz.gwdg.de/, Application version 27, Jochum et al. 2005). Isotopes of elements such as Al, Ca, Ti, Zr, and La were monitored in individual time-resolved signals to avoid inclusions in garnet during data processing. Ablation and processing methods are given below, with conditions for analyses done at UMaine given in parentheses where different than those at the University of Mainz.

Instrumentation at the University of Mainz consisted of a New Wave Nd:YAG 213 nm laser ablation system equipped with a large format ablation cell coupled to an Agilent 7500ce quadrupole ICP-MS (Jacob 2006). The University of Maine MAGIC Lab (MicroAnalytical Geochemistry and Isotope Characterization Laboratory) housed an ESI NWR193^{UC} 193 nm laser ablation system equipped with a TwoVol2 large format ablation cell, coupled to an Agilent 8900 ICP-MS/MS. Garnet was ablated using 12 (15) μm round spots with a beam energy density of ~ 7 (2.2) J/cm^2 and a repetition rate of 20 (5) Hz using He as the carrier gas. Each analysis consisted of 20 s (15 s) background measurement during laser warmup, 20 s (15 s) of ablation, and 10 s of washout. The following isotopes were monitored: ^{24}Mg, ^{27}Al, ^{29}Si, ^{44}Ca, (^{45}Sc), ^{47}Ti, ^{55}Mn, (^{56}Fe), ^{89}Y, ^{90}Zr (Mainz only), ^{140}Ce (Mainz only), ^{141}Pr, ^{146}Nd, ^{147}Sm, ^{153}Eu, ^{157}Gd, ^{159}Tb, ^{163}Dy, ^{165}Ho, ^{166}Er, ^{169}Tm, ^{172}Yb, ^{175}Lu. Dwell time for all isotopes was 10 ms, except for ^{147}Sm, ^{153}Eu, ^{157}Gd, and ^{175}Lu at the University of Mainz (30 ms). For calibration, NIST SRM 610 (GSD-1G) was analyzed at the beginning and after every 15–50 unknowns. Time-resolved signals were processed using the Trace Elements IS data reduction scheme in Iolite v3.63 (v3.75) (Paton et al. 2011) using ^{29}Si as the internal standardization element based on microprobe values and NIST SRM 610 (GSD-1G) as the calibration material, applying the reference values of Jochum et al. (2011). Reference glasses USGS BCR-2G and GSD-1G (BHVO-2G) were run as quality control materials; measured concentrations were indistinguishable from reference values within uncertainties (see Online Resource 2 Table S1 for quality assurance/quality control data). Measured concentrations for BCR-2G are the same within 1 S.E. analytical uncertainty for the Mainz and Maine laboratories (Tables S1 and S2).

Trace element maps of Yb, Dy, and Eu of a vein-edge garnet (Grt7) in sample RM-1C were collected at the University of Maine. The mapping setup consisted of the ESI dual concentric injector (DCI) fast washout tubing and ICP-MS torch. The He carrier gas flow rate was 1.1 L/min; all other ICP-MS parameters were the same as for spot analyses. A 5×5 μm square spot was rastered in parallel lines across the garnet with a scan speed of 62 μm/s, a beam energy density of 6 J/cm^2, and repetition rate of 150 Hz, for a total acquisition time of ~ 1 h 40 min. The total ICP-MS duty cycle was 80 ms (counting times were 1 ms on Si, 30.4 ms on Eu, 14 ms on Dy, and 19 ms on Yb), which was synchronized to the laser pulse width of 40 ms, resulting in 2 laser pulses per duty cycle. This synchronization of ICP-MS and laser parameters was optimized based on Van Malderen et al. (2018) and van Elteren et al. (2019), and resulted in a pixel size of 5×5 μm for trace element maps. Two lines of glass NIST SRM 610 were rastered using the same conditions as garnet at the beginning and end of the garnet data collection. Time-resolved signals were processed using the Trace Elements DRS in Iolite4 (v4.4.4) using ^{29}Si as the internal calibration element and NIST SRM 610 as the calibrant material. An average concentration of 17.5 wt % Si was applied to the entire map; thus, the concentrations in other minerals in the map are not the true concentrations for those minerals, but the concentrations in garnet are fully quantified. Initial trace element maps were produced using CellSpace in Iolite 4 (Woodhead et al. 2007; Paton et al. 2011; Paul et al. 2012). Final maps were processed in XMapTools (Lanari et al. 2014, 2018).

Secondary Ion Mass Spectrometry (SIMS)

Thin sections of samples RM-1C and 13TIB3 were cut into 25 mm rounds for oxygen isotope analysis by ion microprobe. Target grains were within 5 mm of the center of the mount. A small hole (~ 0.5 mm) was drilled near the center of each round, and multiple pieces of garnet oxygen isotope reference material UWG-2 (δ^{18}O = 5.80 ‰ VSMOW, Valley et al. 1995) were embedded in epoxy in the hole and then polished until they were co-planar with the sample surface. Locations in garnet cores, mantles, and rims were chosen based on zoning in BSE images and major and trace element zoning.

Oxygen isotope ratios were determined using a CAMECA ims-1280 multicollector ion microprobe at the WiscSIMS Facility at the University of Wisconsin-Madison (Kita et al. 2009; Valley and Kita 2009). Samples were cleaned and gold coated prior to analysis. A 2–3 nA Cs+ primary ion beam with 20 kV total accelerating voltage was focused on the sample surface with a beam diameter of ~ 12 μm. Ions for ^{16}O$^-$, ^{16}OH$^-$, and ^{18}O$^-$ were measured with three Faraday cup detectors. Background corrected ^{16}OH$^-$/^{16}O$^-$ ratios serve to monitor OH in garnet and to guard against hydrous inclusions (Wang et al. 2014). Four analyses of UWG-2 were run before and after every ~ 10 sample analyses (Table S16).

Sample analyses were corrected for instrumental bias and drift using the bracketing eight analyses of UWG-2 and a correction for matrix effects. The reproducibility of UWG-2 ranged from 0.11 to 0.48 ‰ (2 S.D.) A single bracket with uncertainty of 0.8 ‰ (2 S.D.) was repeated (Table S16). Matrix effects due to Ca composition in garnet were corrected for using the method of Page et al. (2010). A calibration curve that compositionally brackets the sample garnets was established using reference materials R-53 and GrsSE (Page et al. 2010) and UWPrp-1 (Kitajima et al. 2016) at the beginning of the analysis session (Table S16). Although an instrumental bias effect from Mn concentration has been documented (Martin et al. 2014), the effect is not as consistently observed as the Ca-related bias (Vho et al. 2020c). In the present study, three (3) sample analyses have spessartine concentrations greater than 10 mol % (10.7, 18.6, and 18.9%) where a Mn correction might be appropriate.

However, there is no correlation between Mn and oxygen isotope ratio in these data, so a secondary Mn correction was deemed unnecessary. Compositional bias due to a Ca correction is estimated to have an uncertainty of 0.3 ‰ (2 S.D., Page et al. 2010), which, when added in quadrature to the analytical precision, results in a range of 0.32–0.57 ‰ (2 S.D.). Oxygen isotope ratios are reported as delta values (δ^{18}O, ‰) relative to VSMOW (Vienna Standard Mean Ocean Water).

Analytical results

Major element chemistry

Major element maps for matrix and vein-edge garnet can be found in Figs. 2, 3 and 4 and Online Resource 1 (ESM1.
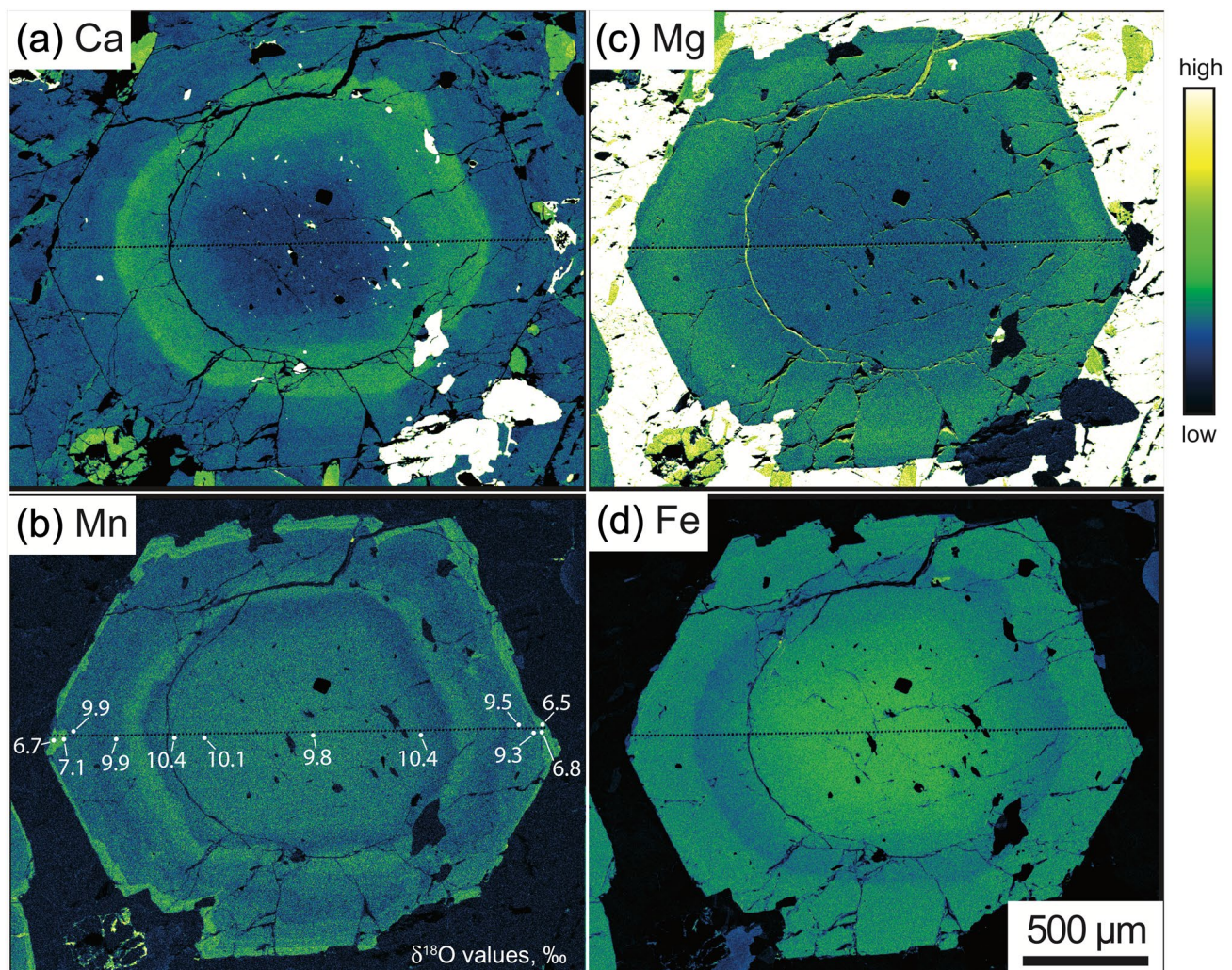

Fig. 3 EDS major element maps of matrix Grt2, sample RM-1C. **a** Ca map. **b** Mn map. **c** Mg map. **d** Fe map. δ^{18}O analysis locations and values (‰) are shown with white circles on the Mn map
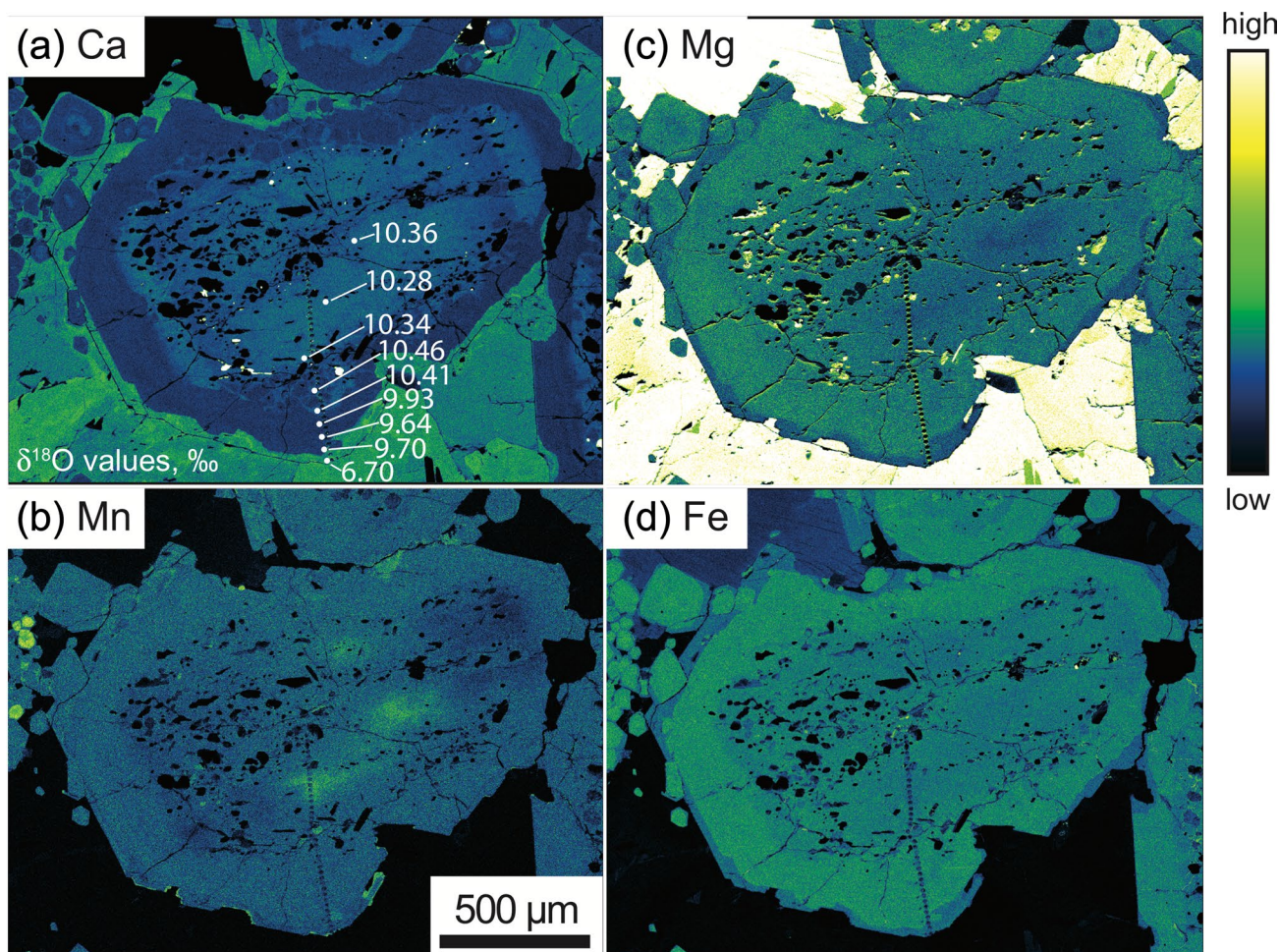
Fig. 4 Images and EDS major element maps of matrix GrtD, sample 13TIB3. **a** XPL. **b** BSE. **c** Ca map. **d** Mn map. **e** Mg map. **f** Fe map. $\delta^{18}O$ analysis locations and values (‰) are shown with white circles on the Ca map

pdf, Figs. S8–S10). Major element concentrations in garnet, amphibole, and white mica are summarized in Online Resource 2 (ESM2.xlsx, Tables S3–S11). Amphibole compositions are typically barroisite and magnesiohornblende with actinolitic rims and late glaucophane overgrowth (see Online Resource 1, Figs. S1 and S7). White mica generally has high Si contents (3.44–3.58 Si p.f.u.; Table S4).

Garnet in RM-1C and 13TIB3 is Fe-rich, with a range of 48–61 % almandine in both matrix and vein garnet. Matrix garnet has a relatively restricted range of spessartine contents (2–9 wt. %), with some of the highest values occurring in the outermost rims of grains. Vein garnet has an exceptionally wide range of spessartine contents, from 5 to 26 wt. %, with higher spessartine contents in vein garnet cores, and lower spessartine in vein garnet rims. Oscillatory zoning is observed in Mn in matrix garnet in sample RM-1C (Grt2, Fig. 3), and both Ca and Mn in vein-edge garnet (Fig. 2; e.g., Dudley 1969). Vein-edge garnet displays sector zoning, for instance, in the inner mantle, and is visible in BSE and

major-element maps (Fig. 2). Individual vein garnet grains show clear core, mantle, and rim zones that can been seen in the BSE images and the major element zoning (Fig. 1h). The garnetite veins are also zoned in their major element composition perpendicular to the length of the vein (Figs. 1, S2, S4, S8; see also the supplementary material of Mulcahy et al. 2018).

Major element zoning in matrix garnet in samples RM-1C and 13TIB3 is consistent with that reported by Mulcahy et al. (2018); that is, two general types of zoning patterns are observed. Some garnet grains have cores that are higher in Fe and Mn and lower in Ca and Mg compared to the surrounding mantle (RM-1C Grt2, Fig. 3), whereas others have cores that are higher in Ca and Mn and lower in Mg and Fe (13TIB3 GrtD, Fig. 4). Matrix and vein-edge garnets in sample RM-1C have a Mn annulus in the garnet mantle, possibly the result of resorption. All matrix garnet grains have a Mn-enriched outermost Mn rim; this is most prominent in

sample RM-1C (Fig. 3), but can also been seen at the very edges of GrtD in 13TIB3 (Fig. 4).

Trace element chemistry

Trace element concentrations in garnet and rutile in all samples can be found in Online Resource 2 (Tables S12–S14). Zirconium concentrations in rutile in sample RM-1C (Table S12; Cruz-Uribe et al. 2018) can be divided into three groups: those found in garnet cores (Population 1; 63–179 μg g^{-1}), those found in garnet mantles and rims (Population 2; 58–266 μg g^{-1}), and those found disseminated in the matrix and garnetite veins (Population 3; 39–281 μg g^{-1}). Zirconium-in-rutile thermometry presented in Table S12 and in the supplementary text are based on the calibration of Tomkins et al. (2007). Our preferred Zr-in-rutile temperatures are 624 ± 20 °C for Population 1, 620 ± 20 °C for Population 2, and 558 ± 20 °C for Population 3 (see Online Resource 1 for details). Zr-in-rutile temperatures and petrologic observations are consistent with (1) relatively isothermal decompression from eclogite to eclogite–amphibolite conditions, remaining in the rutile stability field, followed by (2) relatively isobaric cooling from eclogite–amphibolite to blueschist conditions, associated with overgrowth of rutile by titanite (Fig. S19).

Trace element traverses across garnets are shown in Figs. 5, 6, 7, 8 and S12–S15. Profiles of Lu, Er, Dy, and Eu are shown as representative of the HREE to lighter MREE, respectively. Trace element maps of Yb (mimics Lu and other HREE), Dy, and Eu in vein-edge garnet Grt7 are shown in Fig. 9. Matrix garnet in sample RM-1C (Grt2) has a core that shows increasing HREE from the center outward, followed by a series of oscillations (marked by black arrows, Fig. 5a). The chondrite-normalized REE patterns for this core zone are steep in the MREE to HREE (Fig. 10). The core zone (white, Fig. 5) also shows rimward peaks in progressively lighter REE (Fig. 5a–d), with the REE patterns reflecting enrichment in MREE (Fig. 5e–f); this zone is henceforth referred to as Stage 1 (Fig. 11). The mantle zone in this garnet is characterized by multiple oscillations in REE and a strong enrichment in MREE relative to HREE (mauve, Fig. 5); the mantle zone is deemed Stage 2. Finally, in the outer rim of this garnet, there is an HREE-rich annulus, followed by more oscillations in REE (purple zone, Fig. 5), here called Stage 3.

Matrix garnet in sample 13TIB3 (GrtD) follows the same general patterns in REE (Fig. 6) as does matrix Grt2 in RM-1C (Fig. 5). This garnet has a unique zone (Fig. 6f) in which REE and Ca oscillations occur, coincident with a zone of the garnet that appears to have overgrown many smaller grains, as seen in the Ca map (Figs. 4c and 6d).

Vein-edge garnet in sample RM-1C (Grt3, Grt4, Grt5, Grt7) shows the same patterns as the matrix garnets, but on a smaller scale, as each is only a few hundred microns across (Figs. 7, 9, S12 and S13). Vein-edge garnet cores (Stage 1) are enriched in HREE and have steep MREE to HREE patterns (Figs. 7a, d and 9); these cores are typically inclusion-rich (e.g., Fig. 2a), as are many of the matrix garnet cores. Oscillatory zoning, particularly in MREE, characterizes the vein-edge garnet mantles (Stage 2), and garnet rims are generally more depleted in REE (Stage 3).

Vein garnet is characterized by REE patterns that are enriched in MREE relative to HREE (Figs. 8 and S14). Individual vein garnet grains (for instance, GrtG in sample 13TIB3; Fig. S14) have cores (Stage 1) and mantles (Stage 2) that are more enriched in light (L)REE and MREE relative to HREE than the rims (purple, Stage 3). There is also a wide range in vein garnet grain size, with the larger grains ~ 250 μm and the smaller 5–50 μm; larger vein garnet cores are enriched in MREE relative to HREE (Fig. 8e), whereas the smaller cores have flat chondrite-normalized REE patterns that are flat across the MREEs and HREEs (Fig. 8f). On a broader scale, the veins are zoned in REE; for instance, Fig. 8a shows that Lu is low in the larger vein garnet grains that are at the interior of the vein (left side of traverse), is higher in the part of the vein that has very small garnet grains (central section of traverse), and is low in the outer low-BSE zone (purple; right side of traverse) at the vein edge. At the same time, Eu is high in the vein interior and decreases toward the vein edge (Fig. 8c). It is important to keep in mind that the traverse shown in Fig. 8 represents spots that are a mix of multiple zones of vein garnet (cores, mantles, and rims), particularly in the central section of the traverse. The low-BSE vein garnet "cement" zone (Stage 3) is characterized by lower concentrations of REE overall.

Oxygen isotope ratios

Oxygen isotope data can be found in Tables S16 and S17. Garnet δ^{18}O values in samples RM-1C and 13TIB3 range from 5.3 to 11.1 ‰ (Fig. 11). The cores of all of garnet (Stage 1; matrix and vein) range from 9.8 to 11.1 ‰ (median 10.4 ‰, $n = 21$). A shift to slightly lower values occurs from core to mantle (Fig. 11); this mantle zone ranges from 8.3 to 10.0 ‰ (median 9.7 ‰, $n = 28$). This shift toward slightly lower δ^{18}O values occurs after the Mn annulus identified in RM-1C matrix Grt2. Garnet growth post-annulus typically coincides with other changes in garnet major element chemistry, including Ca and Mg. However, it is unlikely that the difference in δ^{18}O is due to a slight overcorrection of the garnet composition effect in the calculation of δ^{18}O, because the decrease in δ^{18}O is present in garnet that has both higher Ca in the adjacent core (i.e., Grt2, Fig. 5b) and also lower
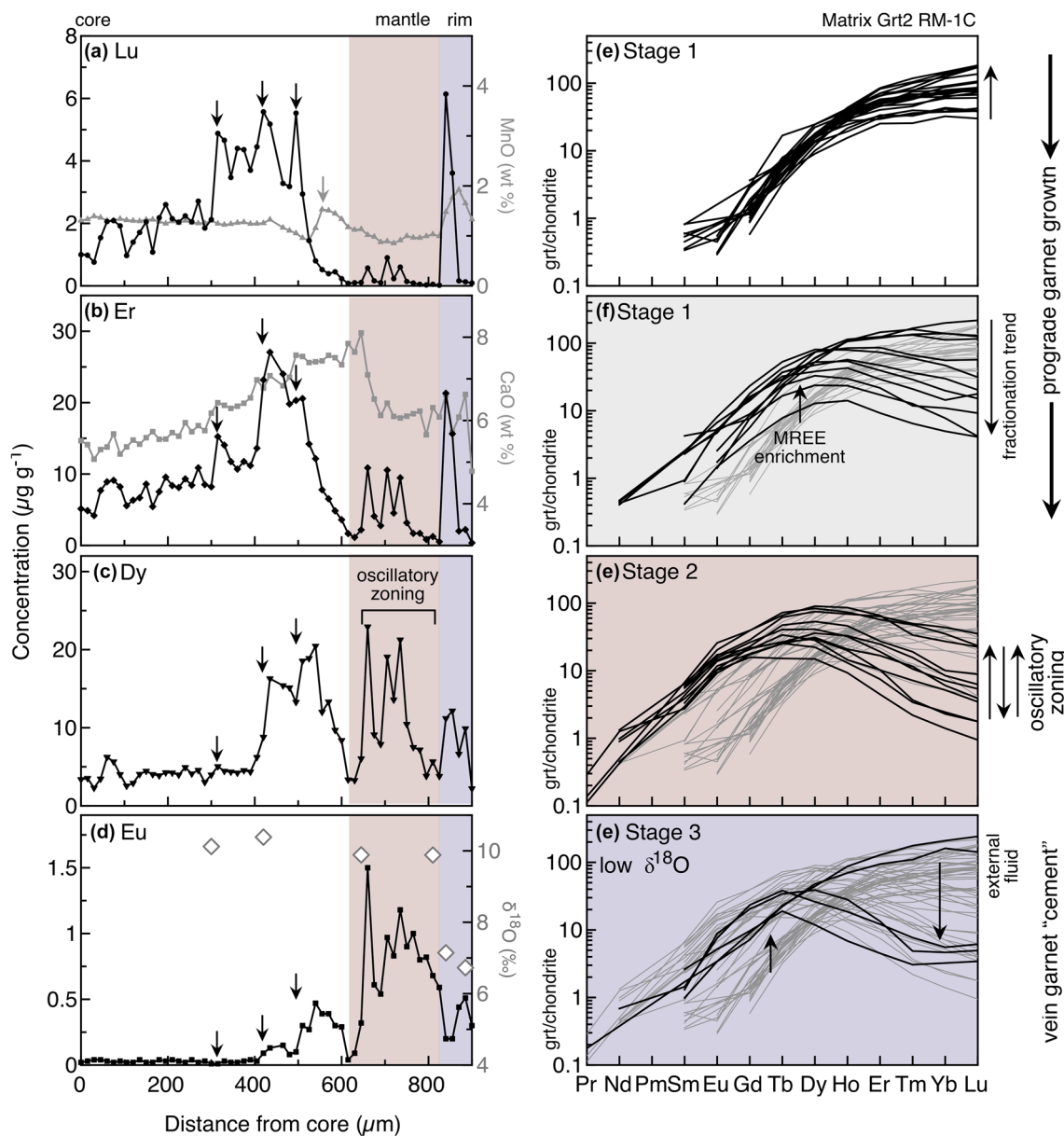
Fig. 5 Core-rim zoning in matrix Grt2 in sample RM-1C. **a–d** Major elements (grey lines, wt % oxide), trace elements (black lines, µg g^{-1}) and δ^{18}O values (diamonds), and **e–h** chondrite-normalized REE patterns. **a** Lu (black filled circles) and MnO (grey filled triangles. **b** Er (black filled diamonds) and CaO (grey filled squares). **d** Dy (black filled inverse triangles). **e** Eu (black filled squares). Chondritic values from Sun and McDonough (1989) in all figures. Garnet growth stages indicated by white (Stage 1), mauve (Stage 2), and purple (Stage 3) backgrounds here and in subsequent figures

Ca in the adjacent core (i.e., Grt3, Fig. 7b). δ^{18}O values in garnet rims in the matrix and vein range from 5.8 to 7.8 ‰ (median 6.7 ‰, $n = 11$), which is distinctly lower than the core and mantle populations.

Discussion

The three stages of garnet growth (Stage 1 cores, Stage 2 mantles, Stage 3 rims + cement) are observed in all three populations of garnet (matrix, vein-edge, and vein). The presence of large-scale (many meters long) vein networks of garnetite through the amphibolitized part of the eclogite block and the consistency in the geochemistry of matrix and vein garnet suggests that fluids were present throughout much of the history of garnet growth. The cores of
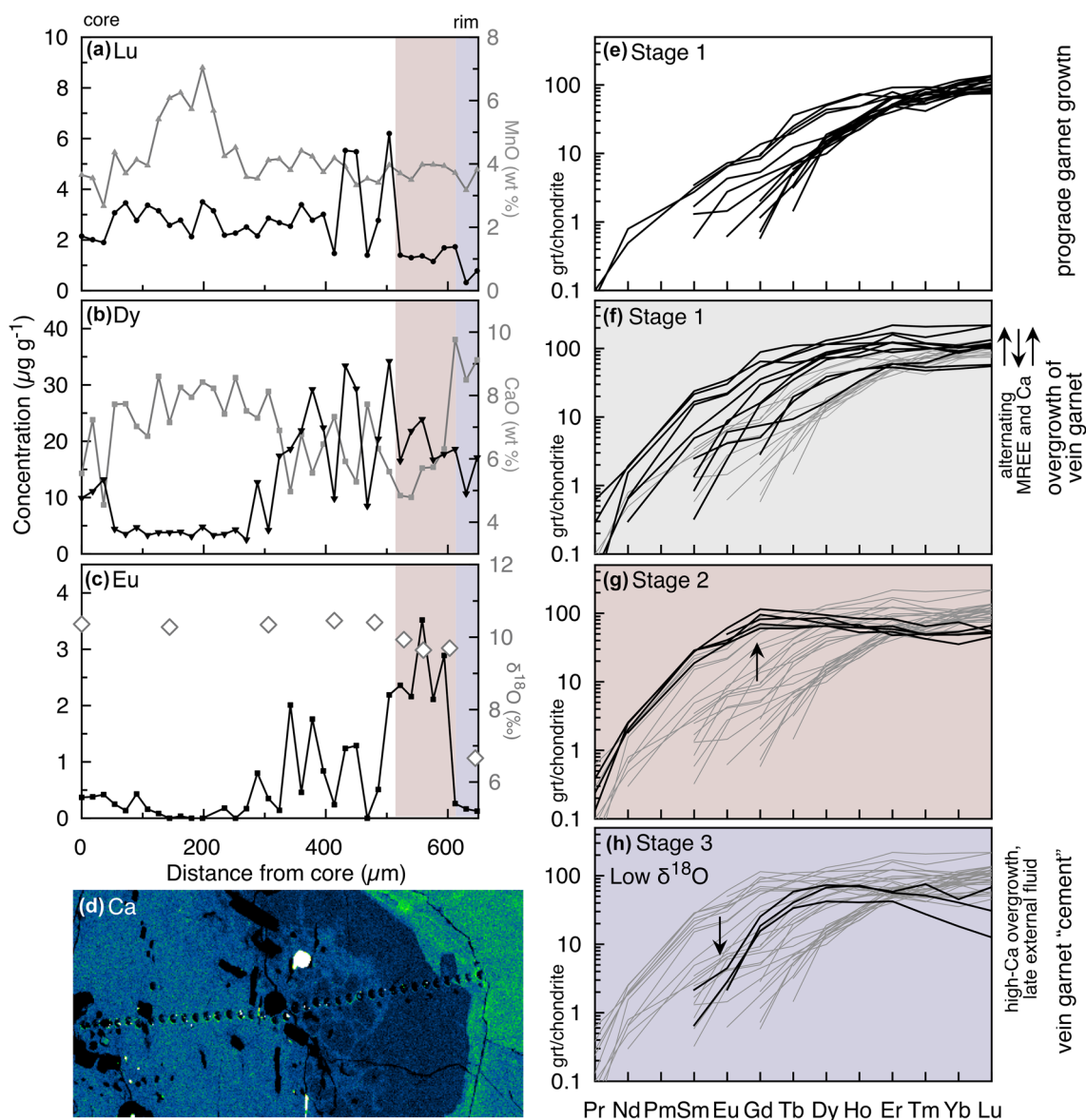
Fig. 6 Core-rim zoning in matrix GrtD in sample 13TIB3. **a–c** Major elements (grey lines, wt % oxide), trace element (black lines, µg g^{-1}), and δ^{18}O values (diamonds), **d** Ca map, and **e–h** chondrite-normalized REE patterns. Symbols as in Fig. 5

vein-edge garnet grains share major and trace element chemistry with the cores of matrix garnets, and vein garnet core chemistry is consistent with the outer core of matrix garnets, which suggests that the garnetite veins were beginning to form during Stage 1 garnet growth. Hence, we invoke fluids as a key component of many of the points discussed below.

Major and trace element zoning in garnet

The major and trace element zoning in matrix Grt2, sample RM-1C, reveals a complex history (Fig. 5; for full rim-to-rim profile see Fig. S15). The core of this garnet does not

contain the classic central peak in HREE (e.g., Hollister 1966; Otamendi et al. 2002), though other matrix garnet grains in the rock do. This garnet is also less inclusion-rich in the core than other matrix garnet in the sample. These features are likely due to either later nucleation compared to other matrix garnet, or slightly asymmetric sectioning in the thin section. The outer core of the garnet has a series of peaks or annuli in the REEs that occur progressively rimward with a decrease in atomic mass of the element. These peaks/annuli could be interpreted as the result of diffusion-limited growth.

Many workers have reflected upon the idea of matrix-diffusion-limited growth in garnet, and its effects on
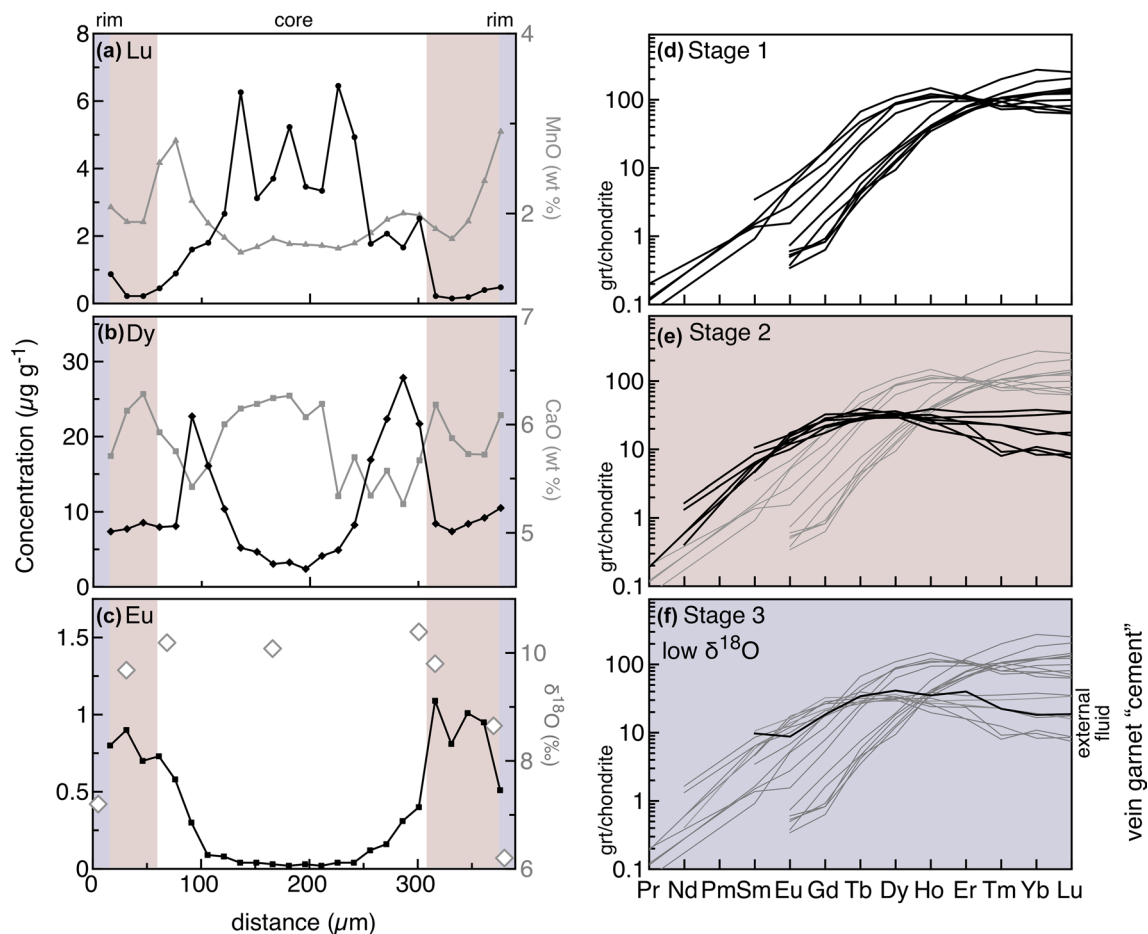
Fig. 7 Rim-to-rim zoning in vein-edge Grt3 in sample RM-1C. **a–c** Major elements (grey lines, wt % oxide), trace element (black lines, µg g^{-1}), and δ^{18}O values (diamonds), and **d–f** chondrite-normalized REE patterns. Symbols as in Fig. 5

trace element patterns, specifically for REEs (e.g., Skora et al. 2006; Moore et al. 2013; Rubatto et al. 2020). The basic tenet of this hypothesis is that diffusion through the matrix is slower for lighter REE than it is for heavier REE, thereby producing peaks in REE in garnet that progress rimward with decreasing atomic number. We suggest that diffusion-limited growth is one controlling factor in the core zones of garnet in sample RM-1C (Figs. 5, 7, S12 and S13). However, we propose a modification to this interpretation, as explained below.

Our first observation is that successively rimward peaks are characterized by progressively lighter REE. Three peaks in Lu within the garnet core (Stage 1, white) are indicated by black arrows in Fig. 5a–d. All three Lu peaks are of approximately the same magnitude. The same peaks occur in Er, Dy, and Eu (and the REE in between), but the core-most peak in Er is far smaller than the next peak rimward; the coremost peak for Dy is very small, the next peak rimward is significant, and the most rimward peak is the most prominent. The same is true for Eu. This first observation

of progressively rimward peaks in lighter REE could be explained by depletion of the REE in the reactive bulk during progressive garnet growth. Because the HREE are the most compatible in garnet, the first garnet that nucleates incorporates a high abundance of HREE, leaving a reactive bulk that is slightly depleted in these elements. The next increment of garnet to grow then has a smaller pool of HREE to draw upon, and so it is relatively enriched in the next lighter REE. This growth, uptake, and depletion progressively depletes the reactive bulk in heavy-to-light REE. Such a process has been proposed to produce a fractionation trend similar to that observed in Fig. 5e–f (e.g., Skora et al. 2006; Konrad-Schmolke et al. 2008). However, these features could also be explained by episodic pulses of fluid release during mineral breakdown (e.g., Taetz et al. 2018), which could cause a shift in the reactive bulk due to spatial and temporal non-uniformity in REE availability. Given the presence of oscillatory zoning and the successively rimward peaks that are characterized by progressively lighter REE,
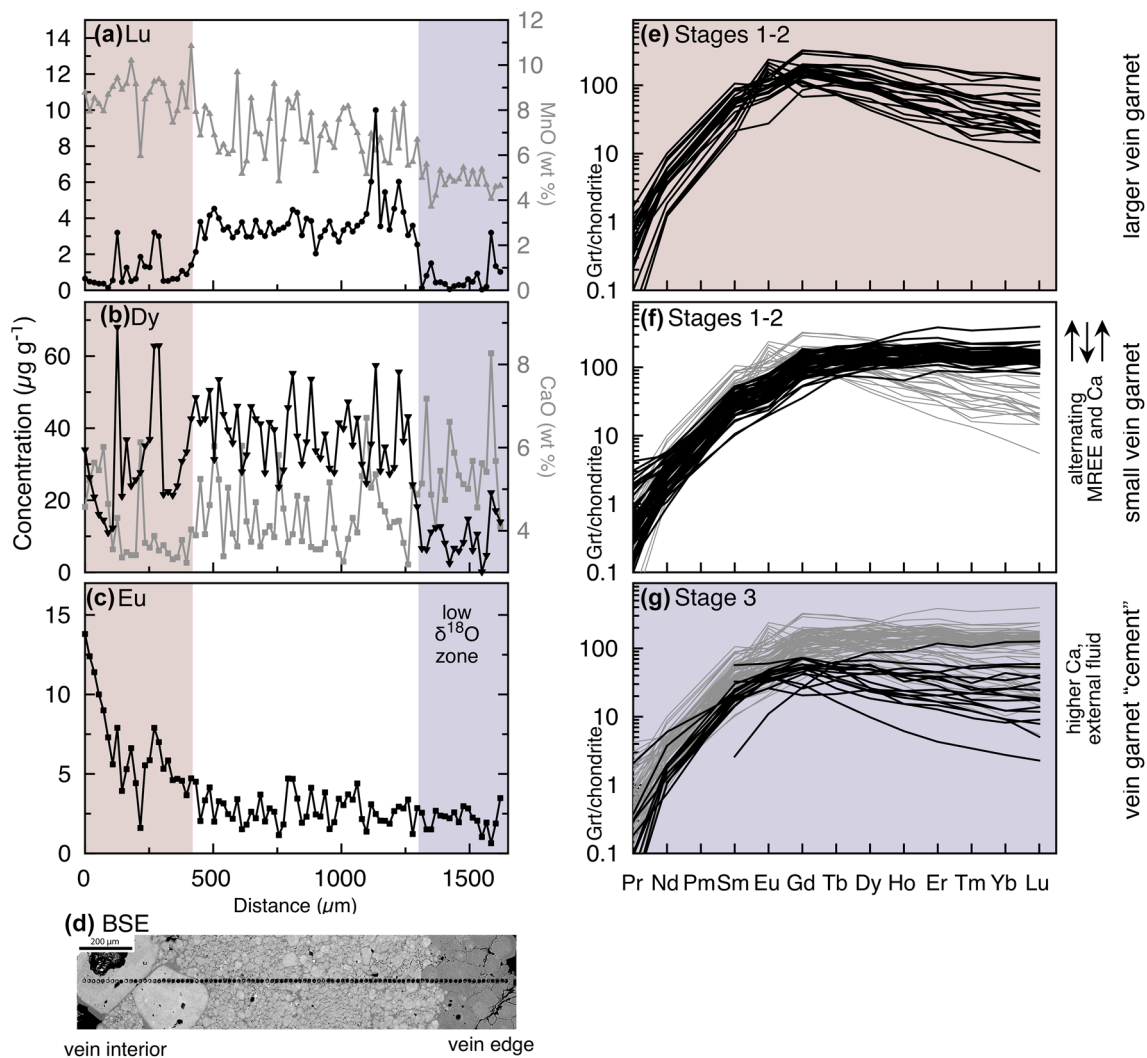
Fig. 8 Zoning across garnetite vein traverse in sample 13TIB3. **a–c** Major elements (grey lines) and trace element (black lines), **d** BSE image, and **e–h** chondrite-normalized REE patterns. Symbols as in Fig. 5

pulses of fluid are highly likely (see subsequent discussion of oxygen isotope data).

The second observation of the core zone of RM-1C matrix Grt2 is that the location of each peak shifts slightly rimward with decreasing atomic number. The arrows designating three peaks in the core in Fig. 5a–d are drawn at exactly the same x position in each figure panel. The second and third Er and Dy peaks are 15 µm rimward of the respective peak in Lu. The second and third Eu peaks are even farther rimward. This may reflect diffusion-limited growth in this sample. Reactions in the rock are likely driven by pulses of fluid (e.g., Baxter et al. 2016; Taetz et al. 2018). The presence of fluids can massively increase the diffusivity of ions to a reaction site, enabling garnet growth. When no fluid is present, transport through the intergranular medium is likely to be orders of magnitude slower. In between pulses of fluid are periods of quiescence; these are the diffusion-limited

times. At the same time, the reactive bulk REE budget in the matrix shifts to be more enriched in MREE, because new garnet growth has sequestered the HREE. These mechanisms fully account for both the general trend in rimward migration of the largest peaks in progressively lighter REE and the differences in the exact location of any given peak based on heavy versus light REE.

The coremost part of the mantle zone of RM-1C matrix Grt2 (Stage 2, mauve, Fig. 5) begins rimward of a Mn annulus that we interpret as a resorption feature. We have used this resorption feature to delineate the boundary between Stage 1 (core) and Stage 2 (mantle) growth. Within this mantle zone are a series of oscillations in REE, and a general enrichment in the MREE over the HREE. The oscillatory zoning is likely due to continued pulses of fluid through the rock, which result in changes in the transient permeability
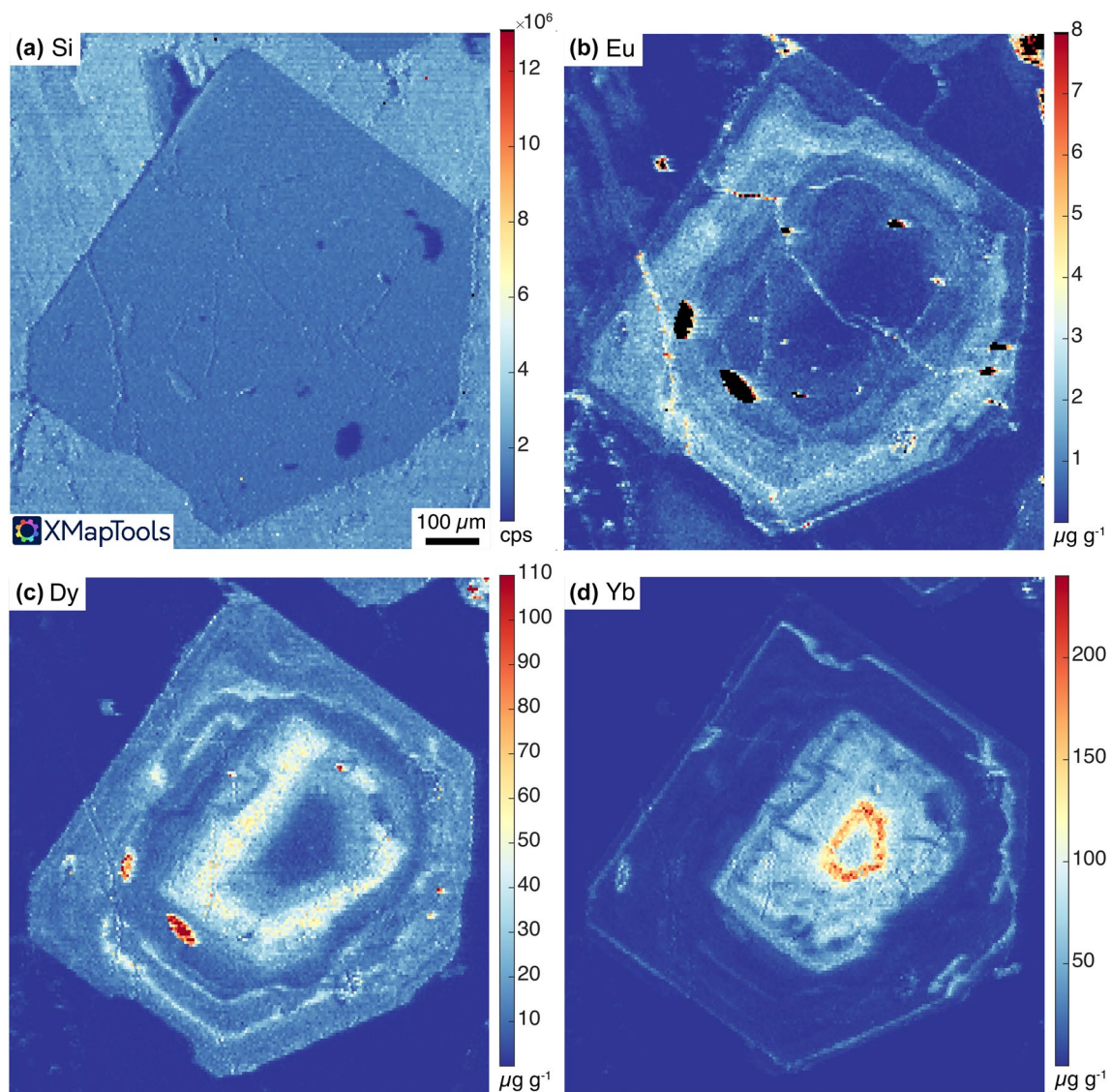
Fig. 9 LA-ICP-MS trace element maps of vein-edge Grt7, sample RM-1C. **a** Raw signal intensity map of Si, counts per second (cps). **b–d** Quantified Eu, Dy, and Yb trace element maps. Color scale for each map indicates concentrations in µg g^{-1}. Cooler colors indicate lower concentration and warmer colors indicate higher concentration

of the rock and cyclic trace element zoning (e.g., Yardley et al. 1991).

The mantle region of RM-1C matrix Grt2 is overgrown by a rim that has an abrupt peak in HREE and an increase in Mn (Stage 3, purple, Fig. 5). This re-enrichment in HREE is consistent with an influx of an externally sourced fluid or the breakdown of a new, HREE-bearing phase, or both (see subsequent discussion of oxygen isotope data). The oscillatory, pulsed nature of garnet growth continues in this outer rim zone, with a second peak that is not present in the HREE but can be seen in Er and Dy, and is the only Eu peak in Stage 3. We interpret this shift from HREE- to MREE-enriched trace element patterns in garnet to be the result of progressive fractionation during garnet growth.

Fluids and oxygen isotopes

The oxygen isotope systematics in garnet provide a framework to integrate the various features of the major and trace element geochemistry. The cores, mantles, and rims of all garnet in both samples (RM-1C and 13TIB3) show the same zoning patterns in $\delta^{18}O$. $\delta^{18}O$ values of garnet cores (Stage 1) range from 9.8 to 11.1 ‰ (median 10.4 ‰). Garnet mantles (Stage 2) shift to slightly lower $\delta^{18}O$ values of 8.3–10.0 ‰ (median 9.7 ‰; Fig. 11).
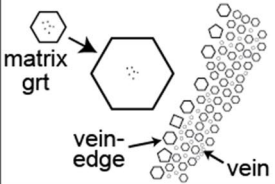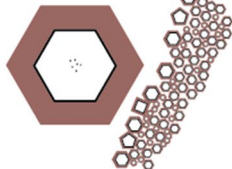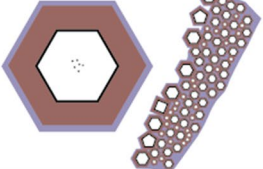
Stage 1 Garnet cores nulceate and grow		Stage 2 Garnet mantles grow post-hiatus	Stage 3 Garnet rims grow, including vein garnet cement
	matrix grt vein-edge → vein		
Geochemistry as defined by RM-1C matrix Grt2	Steep REE patterns, classic fractionation trend of decreasing HREE	MREE>HREE; oscillatory REE zoning	Increase in Mn; re-enrichment of HREE; oscillatory REE zoning
Garnet $\delta^{18}O$	9.8–11.1 ‰ (median 10.4 ‰)	8.3–10.0 ‰ (median 9.7 ‰)	5.8–7.8 ‰ (median 6.7 ‰)

(Vertical label between Stage 1 and Stage 2 columns: "Garnet resorption - Mn Annulus")

Fig. 10 Schematic diagram outlining the three stages of garnet growth, and the chemical signatures typical of each stage

Given the relative similarity in $\delta^{18}O$ values of Stages 1 and 2, it is likely that the fluids present during core and mantle garnet growth in the matrix and vein were internally derived or derived from a protolith with a similar oxygen isotope composition. The $\delta^{18}O$ values in Stages 1 and 2 are consistent with the range of $\delta^{18}O$ values expected of a basalt protolith that experience low-temperature hydrothermal alteration with seawater, as is observed for garnet in metabasalt from Sifnos with reported $\delta^{18}O$ values of 9.2–11.5 ‰ (Putlitz et al. 2000). The shift in $\delta^{18}O$ values between Stages 1 and 2 could also be explained by a change in mineralogy in the bulk rock (e.g., Martin et al. 2014; Vho et al. 2020a); this is consistent with internally-derived pulses of fluid.

Stage 3 garnet, which includes the rims of all garnet and the garnet "cement" in the garnetite veins, has distinctly lower $\delta^{18}O$ values (5.8–7.8 ‰, median 6.7 ‰) than earlier garnet. As the primary phases in the rock (garnet,

omphacite, calcic amphibole) could only account for perhaps 1 ‰ fractionation (e.g., Martin et al. 2014), it is unlikely that a change in mineralogy would have provided sufficient leverage to explain the lower $\delta^{18}O$ values of Stage 3. The shift in $\delta^{18}O$ values from Stage 2 to Stage 3 indicates involvement of a fluid source that was external to the rock. We suggest that the most likely candidate for the source of this low $\delta^{18}O$ signature is the serpentinite mélange. King et al. (2003) reported $\delta^{18}O$ values of 6.3–8.1 ‰ for Franciscan serpentinite separates from Jade Cove and Sand Dollar Beach. Peridotite phases from these localities are consistent with mantle values (Mattey et al. 1994), with $\delta^{18}O$ values of 5.32 ‰ reported for olivine and 5.96 ‰ for clinopyroxene (King et al. 2003). Barnes et al. (2013) reported $\delta^{18}O$ values of 6.0–7.3 ‰ for Franciscan serpentinites from Ring Mountain and the Tiburon Peninsula.

The amphibolitization and development of the blackwall on the block studied here is similar to other blocks at Ring Mountain; blackwall rinds are characterized by actinolite, talc, and white mica, consistent with interaction with serpentinites. The oxygen isotope composition of Stage 3 garnet growth (garnet rims and garnetite "cement") is consistent with interaction with the surrounding serpentinite mélange. These observations are similar to those of Errico et al. (2013) for $\delta^{18}O$ in Franciscan garnet from three localities, including Ring Mountain, for which they reported core-to-rim decreases in $\delta^{18}O$. The low-$\delta^{18}O$ zones likely reflect the point at which the block was physically removed from a larger, more coherent piece of subducted oceanic crust and was incorporated into the mélange, allowing access for new fluids derived from the serpentinite to take advantage of the vein structures that were already present in the rock.
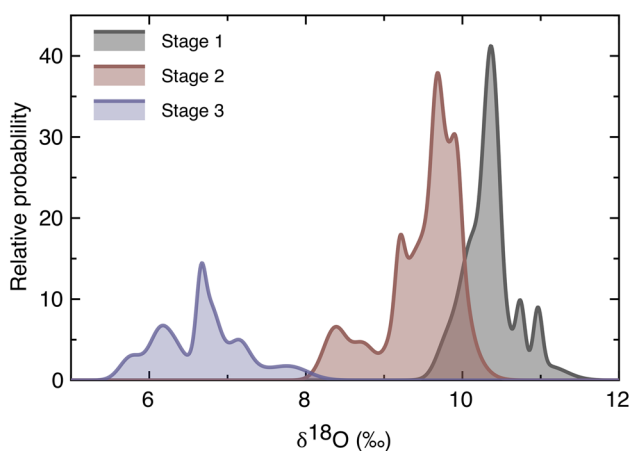
Fig. 11 Probability density plot of $\delta^{18}O$ values for Stage 1 (grey), Stage 2 (mauve), and Stage 3 (purple) garnet growth

A similar story was proposed by Page et al. (2014) for oxygen isotope zoning in Franciscan eclogite from the Junction School locality and hornblendite from Panoche Pass. In the Junction School eclogite, low-$\delta^{18}O$ cores (~ 4 ‰) have higher $\delta^{18}O$ rims (6–7 ‰). At Panoche Pass, high-$\delta^{18}O$ cores (~ 10.9–11.7 ‰) have rims of recrystallized zones with $\delta^{18}O$ values of 8–9 ‰ and outer rims of 6.2–6.8 ‰ (Page et al. 2014). All of these studies, including the present study, point to late-stage garnet rim growth in high-grade blocks under the influence of fluids derived from the Franciscan serpentinite mélange.

Garnetite formation

Garnetites are an uncommon, but not unheard-of, component of metabasic terranes (e.g., Nishiyama et al. 2020; Hertgen et al. 2017; Rivalenti et al. 1997; Xie et al. 2004). One of the most striking optical features of the garnet in these samples, particularly the garnetites and vein-edge garnet, is the presence of birefringent zones (Figs. 2, S3, S5 and S6). Recent work showed that birefringent garnet in blueschists from the Franciscan Complex and Corsica, and phyllites and micaschists from the eastern and central Italian Alps, can be attributed to tetragonal crystal structure (Cesare et al. 2019). We suggest that our birefringent garnets are likely due to a similar process. There are some notable similarities and differences between the garnet reported here and those reported by Cesare et al. (2019), which are outlined below.

In samples shown here, birefringent zones in garnet are clearly visible in a standard 30 µm thin section, particularly in the vein and vein-edge garnet, though birefringent zones are also visible in the rims of the matrix garnet. Cesare et al. (2019) did show one example of birefringent garnet that was visible in a standard thin section, but most of the samples they investigated required a 100 µm-thick section for birefringence to be noticeable. We also observe sector zoning in the garnets from Ring Mountain. The sector zones in our samples correspond to differences in chemistry, whereas Cesare et al. (2018) reported that their optical sector zones did not correspond to chemical discontinuities. The sector zoning, for instance, in RM-1C Grt6 is very clearly visible in the maps of Mn, Mg, and Fe (Fig. 2). The samples in this study are also higher in metamorphic grade (eclogite–amphibolite facies, as opposed to the blueschist–facies and lower in Cesare et al. 2019). Our garnets also have higher pyrope contents (12–22 % Py) than those in Cesare et al. (1–11 % Py).

Similar to Cesare et al., the garnet in this study is anhydrous. During SIMS analyses, we monitored $^{16}OH^-/^{16}O^-$ ratios to monitor OH in garnet and avoid hydrous mineral inclusions. Background corrected $^{16}OH^-/^{16}O^-$ ratios in the hydrospessartine reference material are ~ 4×10^{-3}; the garnet in this study has background

corrected $^{16}OH^-/^{16}O^-$ ratios that are ~ 2 orders of magnitude lower, so it is likely that the birefringence is due to tetragonal structure (Cesare et al. 2019), as opposed to the birefringence reported for hydrogrossular garnets (Rossman and Aines 1991). Confirmation of this difference in structure is evident in cross-polarized light photomicrographs with the lambda plate inserted (Figs. 2, S3, S5 and S6), which highlight the structural anisotropy of the birefringent zones compared to the isotropic zones of garnet.

Perhaps the most intriguing aspect of the garnetite veins is the garnet "cement" that forms a connective medium between the vein garnet cores (Figs. 1g–h and S4). The garnet cement is typically low in BSE intensity compared to the garnet vein cores, due to lower Fe and Mn and higher Ca contents, and forms a fairly significant zone at the edge of the vein in sample 13TIB3 (Fig. S4). The garnet cement is somewhat similar to the honeycomb garnet structures identified in eclogite–facies metasediments from the Tauer Window, Austria (Hawkins et al. 2007), though the honeycomb garnets in that study do not manifest as veins as they do in this study, instead showing evidence of precipitation around quartz grains.

More recently, there have been studies of amorphous phases as mediators for dissolution–reprecipitation reactions (e.g., Keller et al. 2006; Hellmann et al. 2012; Konrad-Schmolke et al. 2018). Essentially, when minerals grow, there are short-lived transient structures that then progress into crystallizing typical mineral structures. The permeability of an amorphous phase is high, but when it crystallizes into a mineral, it becomes relatively impermeable, akin to the precipitation of quartz veins during hydrothermal fluid convection (e.g., Scott and Driesner 2018). These kinds of processes would tend to create monomineralic rocks such as garnetites, omphacitites, or even quartz veins. Konrad-Schmolke et al. (2018) showed that these amorphous phases have a much higher capacity to carry ions than do aqueous fluids, thereby drastically increasing transport and reaction rates. It is unlikely that garnet would precipitate in this manner (as a cement) from an aqueous fluid, as the total dissolved solids (TDS) in aqueous fluids in subduction zones below 600 °C are on the order of 30–40 g/kg water (Manning 2004). Konrad-Schmolke et al. (2018) estimated that an amorphous phase could have TDS ~ 140 g/kg water or more, which is five times that of an aqueous fluid. We suggest that it is much more likely that the garnet cement precipitated from an amorphous phase rich in Si, Al, Ca, Mg, and Fe (e.g., Konrad-Schmolke et al. 2018). An amorphous phase would also create a direct link between the reactants and the growth surface, facilitating the cement-like structure observed in the garnetite.

It is also possible that the mantles and rims of the matrix garnets, in addition to the garnetite cement, precipitated from an amorphous phase. Evidence for this comes from

sample 13TIB3 GrtD (Figs. 4 and 6). It is most plainly seen in the Ca map of Fig. 4 between the higher Ca core and lower Ca mantle of this grain, where it appears the garnet overgrew a zone of smaller garnet grains that have the same composition as the mantle (a larger version of this Ca map is provided in Fig. S17). The higher Ca garnet that infiltrates and grows around the small lower Ca grains is similar to a honeycomb-like structure, akin to the cement of the garnetite veins. This also appears elsewhere in the sample, where the late very high-Ca overgrowth rim envelops a number of smaller grains, again with mantles that have the same low Ca as the mantle of GrtD. However, this alternative overgrowth occurs on a much broader scale, as the proportion of small enveloped grains is much lower relative to the honeycomb-type texture.

Conclusions

An amphibolitized eclogite with garnetite veins from Ring Mountain, California, tells an eventful story of garnet growth. Three stages of garnet growth are identified: in Stage 1, garnet cores crystallize and fractionate HREE from the reactive bulk rock. At some point toward the end of core growth, small garnets nucleate along linear features that form the beginnings of the garnetite vein. Garnet growth progressively depletes the surrounding rock in HREE, leading to an enrichment in MREE. A series of offset REE peaks in this zone is consistent with pulsed fluid flow, in which a pulse of fluid promotes reactions in the rock that result in garnet growth; in between pulses are periods of quiescence during which transport though the matrix is diffusion-limited. Oscillatory zoning in trace elements is present through all stages of garnet growth and can be explained by pulses of fluid that change the transient permeability of the rock. The oscillations represent transitions between fluid-buffered and rock-buffered conditions and result in cyclic trace element zoning. A growth discontinuity in Mn marks the beginning of Stage 2 growth, which is also characterized by oscillatory REE zoning and a general enrichment of MREE relative to HREE. We observe new HREE incorporation during Stage 3, along with increased Mn in garnet rims, followed by continued fluid pulses resulting in oscillatory REE zoning.

Oxygen isotope ratios of 9.8–11.1 ‰ in the cores of the garnets (Stage 1) and 8.3–10.0 ‰ in the mantles (Stage 2) are consistent with an altered oceanic crust protolith that underwent low-T hydrothermal alteration in seawater. Garnet rim and vein cement (Stage 3) $\delta^{18}O$ values of 5.8–7.8 ‰ suggest an external source of oxygen during rim growth, consistent with fluid-mediated interaction with mélange serpentinites. We suggest that Stage 3 garnet growth signifies a time when this block was physically incorporated into the mélange matrix, greatly enhancing interaction with surrounding serpentinite.

Stage 3 garnet growth also involved the crystallization of a garnetite cement that effectively glued tiny earlier garnets together into a cohesive vein. We suggest that a possible mechanism for this cementation is crystallization from an amorphous phase. This has far-reaching implications for how major and trace elements are transported at high pressures, and the role of amorphous phases during mineral dissolution and reprecipitation (e.g., Konrad-Schmoke et al. 2018). Additionally, the presence of birefringent zones in garnet is likely due to tetragonal garnet growth. This is one of the first cases of tetragonal garnet growth reported in the amphibole–eclogite facies, and supports the suggestion made by Cesare et al. (2019) that these types of features may be more common than previously thought.

Author contributions The study was conceptualized and designed by Alicia Cruz-Uribe and F. Zeb Page. Material preparation, data collection, and analysis were performed by Alicia Cruz-Uribe, F. Zeb Page, and Emilie Lozier. Data processing was performed by Alicia Cruz-Uribe, F. Zeb Page, and Kouki Kitajima. LA-ICP-MS analyses at the University of Mainz were done in collaboration with Thomas Zack, Dorrit Jacob, and Regina Mertz-Kraus. The first draft of the manuscript was written by Alicia Cruz-Uribe and all authors commented on versions of the manuscript. All authors have approved the final manuscript.

Declarations

Conflict of interest The authors have no conflicts of interest to declare that are relevant to the content of this article.

References

Anczkiewicz R, Szczepanski J, Mazur S, Storey C (2007) Lu–Hf geochronology and trace element distribution in garnet: Implications

for uplift and exhumation of ultra-high pressure granulites in the Sudetes, SW Poland. Lithos 95:363–380

Barnes JD, Eldam R, Lee C-TA, Errico JC, Loewy S (2013) Petrogenesis of serpentinites from the Franciscan complex, western California, USA. Lithos 178:143–157. https://doi.org/10.1016/j.lithos.2012.12.018

Baxter EF, Caddick MJ, Ague JJ, Dragovic B, Pollington AD, Sullivan N (2016) Three kinds of metamorphic pulses: Geodynamic, thermodynamic, kinetic. Geol Soc Am Abstr Programs 48:2016AM – 284910. https://doi.org/10.1130/abs/2016am-284910

Bebout G, Barton M (2002) Tectonic and metasomatic mixing in a high-T, subduction-zone mélange—insights into the geochemical evolution of the slab–mantle interface. Chem Geol 187:79–106. https://doi.org/10.1016/s0009-2541(02)00019-0

Bebout GE, Penniston-Dorland SC (2016) Fluid and mass transfer at subduction interfaces—The field metamorphic record. Lithos 240–243:228–258. https://doi.org/10.1016/j.lithos.2015.10.007

Bero DA (2014) Geology of Ring Mountain and Tiburon Peninsula, Marin County, California. Map Sheet 62, California Geological Survey.

Brothers RN (1954) Glaucophane schists from the North Berkeley Hills, California. Am J Sci 252:614–626. https://doi.org/10.2475/ajs.252.10.614

Catlos EJ, Sorensen SS (2003) Phengite-based chronology of K- and Ba-rich fluid flow in two paleosubduction zones. Science 299:92–95. https://doi.org/10.1126/science.1076977

Cesare B, Nestola F, Johnson T, Mugnaoili E, Della Ventura G, Peruzzo L, Bartoli O, Viti C, Erickson T (2019) Garnet, the archetypal cubic mineral, grows tetragonal. Sci Rep 9:14672. https://doi.org/10.1038/s41598-019-51214-9

Cloos M, Shreve R (1988) Subduction-channel model of prism accretion, melange formation, sediment subduction, and subduction erosion at convergent plate margins: 1 background and description. Pure Appl Geophys 128:455–500. https://doi.org/10.1007/bf00874548

Cruz-Uribe AM, Hoisch TD, Wells ML, Vervoort JD, Mazdab FK (2015) Linking thermodynamic modelling, Lu-Hf geochronology and trace elements in garnet: new P-T-t paths from the Sevier hinterland. J Metamorph Geol 33:763–781. https://doi.org/10.1111/jmg.12151

Cruz-Uribe AM, Feineman MD, Zack T, Jacob DE (2018) Assessing trace element (dis)equilibrium and the application of single element thermometers in metamorphic rocks. Lithos 314–315:1–15. https://doi.org/10.1016/j.lithos.2018.05.007

Dudley PP (1969) Electron microprobe analyses of garnet in glaucophane schists and associated eclogites. Am Miner 54:139–1150

Errico JC, Barnes JD, Strickland A, Valley JW (2013) Oxygen isotope zoning in garnets from Franciscan eclogite blocks: evidence for rock–buffered fluid interaction in the mantle wedge. Contrib Mineral Petrol 166:1161–1176. https://doi.org/10.1007/s00410-013-0915-0

Hawkins A, Selverstone J, Brearley A, Beane RJ, Ketcham RA, Carlson WD (2007) Origin and mechanical significance of honeycomb garnet in high-pressure metasedimentary rocks from the Tauern Window, Eastern Alps. J Metamorph Geol 25:565–583. https://doi.org/10.1111/j.1525-1314.2007.00714.x

Hellmann R, Wirth R, Daval D, Barnes J-P, Pennison J-M (2012) Unifying natural and laboratory chemical weathering with interfacial dissolution–reprecipitation: a study based on the nanometer-scale chemistry of fluid–silicate interfaces. Chem Geol 294:203–216. https://doi.org/10.1016/j.chemgeo.2011.12.002

Hertgen S, Yamato P, Morales LFG, Angiboust S (2017) Evidence for brittle deformation events at eclogite-facies P-T conditions (example of the Mt. Emilius klippe, Western Alps). Tectonophysics 706:1–13. https://doi.org/10.1016/j.tecto.2017.03.028

Hickmott D, Shimizu N, Spear F, Selverstone J (1987) Trace-element zoning in a metamorphic garnet. Geology 15:573–576. https://doi.org/10.1130/0091-7613(1987)15%3c573:tziamg%3e2.0.co;2

Hollister LS (1966) Garnet zoning: an interpretation based on the Rayleigh fractionation model. Science 154:1647–1651

Horodyskyj U, Lee C-TA, Luffi P (2009) Geochemical evidence for exhumation of eclogite via serpentinite channels in ocean-continent subduction zones. Geosphere 5:426–438. https://doi.org/10.1130/ges00502.1

Jacob DE (2004) Nature and origin of eclogite xenoliths from kimberlites. Lithos 77:295–316. https://doi.org/10.1016/j.lithos.2004.03.038

Jacob DE (2006) High sensitivity analysis of trace element-poor geological reference glasses by Laser ablation-Inductively coupled plasma-Mass spectrometry (LA-ICP-MS). Geostand Geoanal Res 30:221–235

Jochum KP, Nohl U, Herwi K, Lammel E, Stoll B, Hofmann AW (2005) GeoReM: a new geochemical database for reference materials and isotopic standards. Geostand Geoanal Res 29:333–338

Jochum KP, Weis U, Stoll B, Kuzmin D, Yang Q, Raczek I, Jacob DE, Stracke A, Birbaum K, Frick DA, Günther D, Enzweiler J (2011) Determination of Reference values for NIST SRM 610–617 glasses following ISO guidelines. Geostand Geoanal Res 35:397–429. https://doi.org/10.1111/j.1751-908x.2011.00120.x

Keller LM, Abart R, Wirth R, Schmid DW, Kunze K (2006) Enhanced mass transfer through short-circuit diffusion: growth of garnet reaction rims at eclogite facies conditions. Am Mineral 91:1024–1038. https://doi.org/10.2138/am.2006.2068

Kelly E, Carlson W, Connelly J (2011) Implications of garnet resorption for the Lu-Hf garnet geochronometer: an example from the contact aureole of the Makhavinekh Lake Pluton, Labrador. J Metamorph Geol 29:901–916. https://doi.org/10.1111/j.1525-1314.2011.00946.x

King RL, Kohn MJ, Eiler JM (2003) Constraints on the petrologic structure of the subduction zone slab-mantle interface from Franciscan complex exotic ultramafic blocks. Geol Soc Am Bull 115:1097–1109

Kita NT, Ushikubo T, Fu B, Valley JW (2009) High precision SIMS oxygen isotope analysis and the effect of sample topography. Chem Geol 264:43–57. https://doi.org/10.1016/j.chemgeo.2009.02.012

Kitajima K, Strickland A, Spicuzza MJ, Tenner TJ, Valley JW (2016) Improved matrix correction of δ18O analysis by SIMS for pyralspite and Cr-pyrope garnets. Goldschm Abst 2016:1542

Kohn MJ, Valley JW (1994) Oxygen isotope constraints on metamorphic fluid flow, Townshend Dam, Vermont, U.S.A. Geochim Cosmochim Ac 58:5551–5566. https://doi.org/10.1016/0016-7037(94)90249-6

Konrad-Schmolke M, Babist J, Handy M, O'Brien P (2006) The physico-chemical properties of a subducted slab from garnet zonation patterns (Sesia Zone, Western Alps). J Petrol 47:2123. https://doi.org/10.1093/petrology/egl039

Konrad-Schmolke M, Zack T, O'Brien PJ, Jacob DE (2008) Combined thermodynamic and rare earth element modelling of garnet growth during subduction: Examples from ultrahigh-pressure eclogite of the Western Gneiss Region, Norway. Earth Planet Sci Lett 272:488–498. https://doi.org/10.1016/j.epsl.2008.05.018

Konrad-Schmolke M, Halama R, Wirth R, Thomen A, Klitscher N, Morales L, Schreiber A, Wilke FDH (2018) Mineral dissolution and reprecipitation mediated by an amorphous phase. Nat Commun 9:1637. https://doi.org/10.1038/s41467-018-03944-z

Lanari P, Vidal O, Andrade VD, Dubacq B, Lewin E, Grosch EG, Schwartz S (2014) XMapTools: a MATLAB©-based program for electron microprobe X-ray image processing and

geothermobarometry. Comput Geosci 62:227–240. https://doi.org/10.1016/j.cageo.2013.08.010

Lanari P, Vho A, Bovay T, Airaghi L, Centrella S (2018) Quantitative compositional mapping of mineral phases by electron probe micro-analyser. Geol Soc London Spec Publ 478:39–63. https://doi.org/10.1144/sp478.4

Manning C (2004) The chemistry of subduction-zone fluids. Earth Planet Sci Lett 223:1–16. https://doi.org/10.1016/j.epsl.2004.04.030

Marschall HR, Schumacher JC (2012) Arc magmas sourced from mélange diapirs in subduction zones. Nat Geosci 5:1–6. https://doi.org/10.1038/ngeo1634

Martin LAJ, Rubatto D, Crépisson C, Hermann J, Putlitz B, Vitale-Brovarone A (2014) Garnet oxygen analysis by SHRIMP-SI: matrix corrections and application to high-pressure metasomatic rocks from Alpine Corsica. Chem Geol 374–375:25–36. https://doi.org/10.1016/j.chemgeo.2014.02.010

Mattey D, Lowry D, Macpherson C (1994) Oxygen isotope composition of mantle peridotite. Earth Planet Sci Lett 128:231–241. https://doi.org/10.1016/0012-821x(94)90147-3

Miller DP, Marschall HR, Schumacher JC (2009) Metasomatic formation and petrology of blueschist-facies hybrid rocks from Syros (Greece): implications for reactions at the slab-mantle interface. Lithos 107:53–67

Moore SJ, Carlson W, Hesse M (2013) Origins of yttrium and rare earth element distributions in metamorphic garnet. J Metamorph Geol 31:663–689. https://doi.org/10.1111/jmg.12039

Mulcahy SR, Starnes JK, Day HW, Coble MA, Vervoort JD (2018) Early onset of Franciscan subduction. Tectonics 37:1194–1209. https://doi.org/10.1029/2017tc004753

Nelson BK (1995) Fluid flow in subduction zones: evidence from Nd- and Sr-isotope variations in metabasalts of the Franciscan complex. Contrib Mineral Petrol 119:247–262. https://doi.org/10.1007/bf00307285

Nishiyama T, Ohfuji H, Fukuba K, Terauchi M, Nishi U, Hrada K, Unoki K, Moribe Y, Yoshiasa A, Ishimaru S, Mori Y, Shigeno M, Arai S (2020) Microdiamond in a low-grade metapelite from a Cretaceous subduction complex, western Kyushu. Japan Sci Rep 10:11645. https://doi.org/10.1038/s41598-020-68599-7

Otamendi J, Rosa JDL, Douce A, Castro A (2002) Rayleigh fractionation of heavy rare earths and yttrium during metamorphic garnet growth. Geology 30:159–162

Page F, Armstrong L, Essene E, Mukasa S (2007) Prograde and retrograde history of the Junction School eclogite, California, and an evaluation of garnet–phengite–clinopyroxene thermobarometry. Contrib Mineral Petrol 153:533–555

Page FZ, Kita NT, Valley JW (2010) Ion microprobe analysis of oxygen isotopes in garnets of complex chemistry. Chem Geol 270:9–19. https://doi.org/10.1016/j.chemgeo.2009.11.001

Page FZ, Essene EJ, Mukasa SB, Valley JW (2014) A Garnet-Zircon oxygen isotope record of subduction and exhumation fluids from the Franciscan complex, California. J Petrol 55:103–131. https://doi.org/10.1093/petrology/egt062

Page FZ, Cameron EM, Flood CM, Dobbins JW, Spicuzza MJ, Kitajima K, Strickland A, Ushikubo T, Mattinson CG, Valley JW (2019) Extreme oxygen isotope zoning in garnet and zircon from a metachert block in mélange reveals metasomatism at the peak of subduction metamorphism. Geology 47:655–658. https://doi.org/10.1130/g46135.1

Paton C, Hellstrom J, Paul B, Woodhead J, Hergt J (2011) Iolite: freeware for the visualisation and processing of mass spectrometric data. J Anal At Spectrom 26:2508. https://doi.org/10.1039/c1ja10172b

Paul B, Paton C, Norris A et al (2012) Cell space: a module for creating spatially registered laser ablation images within the Iolite freeware

environment. J Anal At Spectrom 27:700–706. https://doi.org/10.1039/c2ja10383d

Penniston-Dorland S, Sorensen S, Ash R, Khadke S (2010) Lithium isotopes as a tracer of fluids in a subduction zone mélange: Franciscan Complex, CA. Earth Planet Sci Lett 292:181–190

Putlitz B, Matthews A, Valley JW (2000) Oxygen and hydrogen isotope study of high-pressure metagabbros and metabasalts (Cyclades, Greece): implications for the subduction of oceanic crust. Contrib Mineral Petrol 138:114–126. https://doi.org/10.1007/s004100050012

Pyle JM, Spear FS (2003) Yttrium zoning in garnet: coupling of major and accessory phases during metamorphic reactions. Am Miner 1:1–49

Rivalenti G, Mazzucchelli M, Barbieri M et al (1997) Garnetite-forming processes in the deep crust: the Val Fiorina case study (Ivrea-Verbano Zone, NW Alps). Eur J Mineral 9:1053–1071

Rossman G, Aines R (1991) The hydrous components in garnets: grossular-hydrogrossular. Am Miner 76:1153–1164

Rubatto D, Angiboust S (2015) Oxygen isotope record of oceanic and high-pressure metasomatism: a P-T–time–fluid path for the Monviso eclogites (Italy). Contrib Mineral Petrol 170:44. https://doi.org/10.1007/s00410-015-1198-4

Rubatto D, Burger M, Lanari P, Hattendorf B, Schwarz G, Neff C, Schmidt PK, Hermann J, Vho A, Günther D (2020) Identification of growth mechanisms in metamorphic garnet by high-resolution trace element mapping with LA-ICP-TOFMS. Contrib Mineral Petrol 175:61. https://doi.org/10.1007/s00410-020-01700-5

Russell AK, Kitajima K, Strickland A, Medaris LG, Schulze DJ, Valley JW (2012) Eclogite-facies fluid infiltration: constraints from δ18O zoning in garnet. Contrib Mineral Petrol 165:103–116. https://doi.org/10.1007/s00410-012-0794-9

Scott SW, Driesner T (2018) Permeability changes resulting from quartz precipitation and dissolution around upper crustal intrusions. Geofluids 2018:1–19. https://doi.org/10.1155/2018/6957306

Skora S, Baumgartner LP, Mahlen NJ, Johnson CM, Pilet S, Hellebrand E (2006) Diffusion-limited REE uptake by eclogite garnets and its consequences for Lu–Hf and Sm–Nd geochronology. Contrib Mineral Petrol 152:703–720

Smit MA, Scherer EE, Mezger K (2013) Lu–Hf and Sm–Nd garnet geochronology: Chronometric closure and implications for dating petrological processes. Earth Planet Sci Lett 381:222–233. https://doi.org/10.1016/j.epsl.2013.08.046

Sorensen S, Grossman J (1993) Accessory minerals and subduction zone metasomatism: a geochemical comparison of two mélanges (Washington and California, USA). Chem Geol 110:269–297

Sun SS, McDonough WF (1989) Chemical and isotopic systematics of oceanic basalts: implications for mantle composition and processes. Geol Soc London Spec Publ 42:313–345. https://doi.org/10.1144/gsl.sp.1989.042.01.19

Taetz S, John T, Bröcker M et al (2018) Fast intraslab fluid-flow events linked to pulses of high pore fluid pressure at the subducted plate interface. Earth Planet Sci Lett 482:33–43. https://doi.org/10.1016/j.epsl.2017.10.044

Tomkins H, Powell R, Ellis DJ (2007) The pressure dependence of the zirconium-in-rutile thermometer. J Metamorph Geol 25:703–713

Tsujimori T, Matsumoto K, Wakabayashi J, Liou JG (2006) Franciscan eclogite revisited: reevaluation of the P-T evolution of tectonic blocks from Tiburon Peninsula, California, U.S.A. Miner Petrol 88:243–267. https://doi.org/10.1007/s00710-006-0157-1

Valley J, Kita N (2009) In situ oxygen isotope geochemistry by ion microprobe. Miner Assoc Canada Short Course 41:19–61

Valley JW, Kitchen N, Kohn MJ, Niendorf CR, Spicuzza MJ (1995) UWG-2, a garnet standard for oxygen isotope ratios: Strategies for high precision and accuracy with laser heating. Geochim

Cosmochim Ac 59:5223–5231. https://doi.org/10.1016/0016-7037(95)00386-x

van Elteren JT, Šelih VS, Šala M (2019) Insights into the selection of 2D LA-ICP-MS (multi)elemental mapping conditions. J Anal Atom Spectrom 34:1919–1931. https://doi.org/10.1039/c9ja00166b

Van Malderen SJM, van Elteren JT, Šelih VS, Vanhaecke F (2018) Considerations on data acquisition in laser ablation-inductively coupled plasma-mass spectrometry with low-dispersion interfaces. Spectrochimica Acta Part B Atomic Spectrosc 140:29–34. https://doi.org/10.1016/j.sab.2017.11.007

Vho A, Lanari P, Rubatto D, Hermann J (2020a) Tracing fluid transfers in subduction zones: an integrated thermodynamic and δ18O fractionation modelling approach. Solid Earth 11:307–328. https://doi.org/10.5194/se-11-307-2020

Vho A, Rubatto D, Lanari P, Francesco G, Regis D, Hermann J (2020b) Crustal reworking and hydration: insights from element zoning and oxygen isotopes of garnet in high-pressure rocks (Sesia Zone, Western Alps). Contrib Miner Petrol 175(11):109. https://doi.org/10.1007/s00410-020-01745-6

Vho A, Rubatto D, Putlitz B, Bouvier A-S (2020c) New reference materials and assessment of matrix effects for SIMS measurements of oxygen isotopes in garnet. Geostand Geoanal Res 44:459–471. https://doi.org/10.1111/ggr.12324

Vielzeuf D, Veschambre M, Brunet F (2005) Oxygen isotope heterogeneities and diffusion profile in composite metamorphic-magmatic garnets from the Pyrenees. Am Mineral 90:463–472. https://doi.org/10.2138/am.2005.1576

Wakabayashi J (1990) Counterclockwise P-T-t Paths from Amphibolites, Franciscan Complex, California: Relics from the Early Stages of Subduction Zone Metamorphism. J Geol 98:657–680. https://doi.org/10.1086/629432

Wang X-L, Coble MA, Valley JW, Shu X-J, Kitajima K, Spicuzza MJ, Sun T (2014) Influence of radiation damage on late Jurassic zircon from southern China: evidence from in situ measurement of oxygen isotopes, laser Raman, U-Pb ages, and trace elements. Chem Geol 389:122–136

Woodhead JD, Hellstrom J, Hergt JM et al (2007) Isotopic and elemental imaging of geological materials by laser ablation inductively coupled plasma-mass spectrometry. Geostand Geoanal Res 31:331–343. https://doi.org/10.1111/j.1751-908x.2007.00104.x

Xie Z, Zheng Y-F, Jahn B, Ballevre M, Chen J, Gautier P, Gao T, Gong B, Zhou J (2004) Sm–Nd and Rb–Sr dating of pyroxene–garnetite from North Dabie in east-central China: problem of isotope disequilibrium due to retrograde metamorphism. Chem Geol 206:137–158. https://doi.org/10.1016/j.chemgeo.2004.01.013

Yang P, Rivers T (2004) The origin of Mn and Y annuli in garnet and the thermal dependence of P in garnet and Y in apatite in calc-pelite and pelite, Gagnon terrane, western Labrador. Am Mineral 88:1398–1398

Yardley BWD, Rochelle CA, Barnicoat AC, Lloyd GE (1991) Oscillatory zoning in metamorphic minerals: an indicator of infiltration metasomatism. Mineral Mag 55:357–365. https://doi.org/10.1180/minmag.1991.055.380.06